SCIENCE CHINA
Chemistry

•ARTICLES•

April 2024 Vol.67 No.4: 1216–1223
https://doi.org/10.1007/s11426-023-1875-7

MOF-based magnetic microrobot swarms for pH-responsive targeted drug delivery

Qinyi Cao[1,2†], Yifan Zhang[1,3†], Yanping Tang[4], Changjin Wu[5], Jizhuang Wang[1,2*] & Dan Li[1,2*]

[1]*College of Chemistry and Materials Science, Jinan University, Guangzhou 510632, China;*
[2]*Guangdong Provincial Key Laboratory of Functional Supramolecular Coordination Materials and Applications, Jinan University, Guangzhou 510632, China;*
[3]*Guangdong Provincial Key Laboratory of Spine and Spinal Cord Reconstruction, The Fifth Affiliated Hospital (Heyuan Shenhe People's Hospital), Jinan University, Heyuan 517000, China;*
[4]*JNU-HKUST Joint Laboratory for Neuroscience and Innovative Drug Research, College of Pharmacy, Jinan University, Guangzhou 510632, China;*
[5]*Department of Chemistry, The University of Hong Kong, Hong Kong, China*

Received September 14, 2023; accepted November 14, 2023; published online February 22, 2024

Metal-organic frameworks (MOFs) hold significant potential as vehicles for drug delivery due to their expansive specific surface area, biocompatibility, and versatile attributes. Concurrently, magnetically actuated micro/nano-robots (MNRs) offer distinct advantages, such as untethered and precise manipulation. The fusion of these technologies presents a promising avenue for achieving non-invasive targeted drug delivery. Here, we report a MOF-based magnetic microrobot swarm (MMRS) for targeted therapy. Our approach overcomes limitations associated with a single MNR, including limited drug loading and the risk of loss during manipulation. We select Zeolitic Imidazolate Framework-8 (ZIF-8) as the drug vehicle for its superior loading potential and pH-sensitive decomposition. Our design incorporates magnetic responsive components into the one-pot synthesis of Fe@ZIF-8, enabling collective behaviors under actuation. Tuning the yaw angle of alternating magnetic fields and nanoparticles' amount, the MMRSs with controllable size achieve instantaneous transformation among different configurations, including vortex-like swarms, chain-like swarms, and elliptical swarms, facilitating adaptation to environmental variations. Transported to the subcutaneous T24 tumor site, the MMRSs with encapsulated doxorubicin (DOX) automatically degrade and release the drug, leading to a dramatic reduction of the tumor *in vivo*. Our investigation signifies a significant advancement in the integration of biodegradable MOFs into microrobot swarms, ushering in new avenues for accurate and non-invasive targeted drug delivery.

magnetic microrobot swarm, MOF nanoparticles, magnetic propulsion, pH-responsive drug release, targeted drug delivery

Citation: Cao Q, Zhang Y, Tang Y, Wu C, Wang J, Li D. MOF-based magnetic microrobot swarms for pH-responsive targeted drug delivery. *Sci China Chem*, 2024, 67: 1216–1223, https://doi.org/10.1007/s11426-023-1875-7

1 Introduction

Micro/nano-robots (MNRs) are artificial micro/nano-machines based on active micro/nano-particles [1–3], which become an emerging technology in healthcare [4–7], energy and environment [8–10]. On the basis of material properties, different propulsion methods can be applied to program the motion of MNRs, including magnetic field [11–13], light [14–16], and ultrasonic [17,18]. Magnetic field-propelled MNRs, in particular, are widely applied in biomedicine owing to their precise controllability, minimal disruption,

†These authors contributed equally to this work.
*Corresponding authors (email: jizhuang@jnu.edu.cn; danli@jnu.edu.cn)

complex programmability, and compatibility with biological systems. Moreover, the rational design of the magnetic controlling system can achieve collective motion of magnetic MNRs [19–21] that emulates the intelligent swarming behaviors observed in living systems, such as flocking of birds and schooling of fish, which presents significant advantages over individual MNRs [22–25], including enhanced cargo capacity, navigation complexity and environmental adaptation.

Metal-organic frameworks (MOFs) are increasingly being explored as alternative materials for designing multifunctional nanoreactors (MFNRs), particularly in the field of biomedical drug delivery and cancer therapy, owing to their exceptional characteristics, including a large surface area, excellent design flexibility, and adjustable porosity. Multiple studies [26–30] have highlighted the advantages of MOFs-based materials in bio-related applications. Because of the acidic tumor microenvironment and the sensitivity of coordination bonds to external pH, the pH-responsive ZIF-8 is widely investigated for cancer therapy and possesses good anticancer efficacy. Moreover, the biocompatibility is also verified there. For instance, ZIF-8, an extensively investigated MOF, has demonstrated synergistic treatment of cancers in view of its low cytotoxicity and pH-responsive degradability in a biological acidic microenvironment [31–35]. Very recently, the ZIF-8-based microrobots have been exploited for active drug delivery through loading ZIF-8 nanoparticles on microrobot carriers, like 3D-printed magnetic helix microrobots [36,37]. Despite the progress achieved in fabrication, practical applications necessitate improvements in the facile large-scale synthesis of MOF-based MFNRs. Meanwhile, the direct manipulation of MOF-based microrobot swarms will also be favorable for biocompatibility by avoiding the adoption of unnecessary microrobot carriers.

Herein, we propose the MOF-based magnetic microrobot swarms (MMRSs) as the targeted drug delivery system (Figure 1). Magnetic-perceptive Fe@ZIF-8 nanoparticles were selected for the construction of MMRSs in order to achieve responsive targeted drug delivery, given their facile synthesis, pH sensitivity, and biocompatibility. The DOX-loaded MMRSs were synthesized using a one-pot mineralization approach that enables multimodal transformation, resulting in various configurations such as vortex-like, chain-like, and elliptical, to accommodate environmental variations and enhance tasking abilities through tailored magnetic fields. Then, MMRSs were manipulated to the targeted region in response to the programmable alternating magnetic field. Due to the pH-responsiveness feature of MMRSs, the loaded DOX is fragmented and released in response to the acidic microenvironment (pH=5.5–6.5) associated with the tumor site, ultimately resulting in the distinguished inhibition of the T24 tumor *in vivo*. These findings shed further light on the potential of microrobot swarms as targeted drug delivery vehicles, lending credence to their potential for upcoming clinical applications.

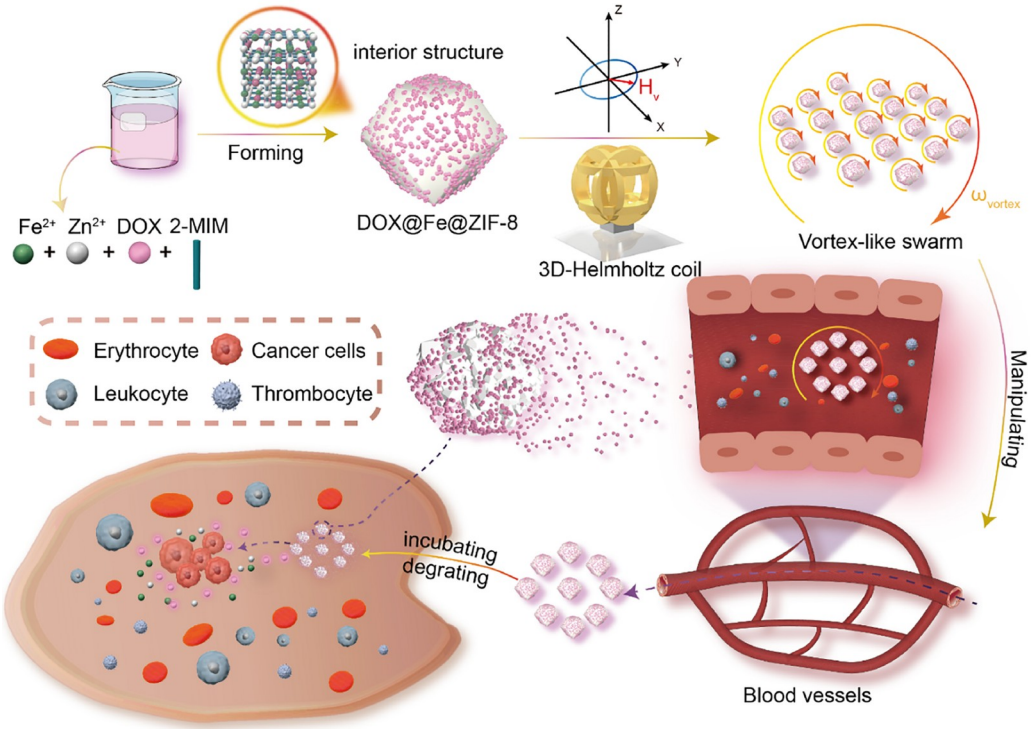

Figure 1 Schematic illustration of forming and manipulating of MMRSs under the tailored magnetic field and pH-responsive drug release (color online).

2 Results

2.1 Fabrication and characterization of Fe@ZIF-8

The magnetic Fe@ZIF-8 nanoparticles were fabricated by the one-pot mineralization method [38], which involves the incorporation of an appropriate ferrous precursor during the synthesis process (see detail in Supporting Information online). As shown in Figure 2a, the as-prepared Fe@ZIF-8 preserved the typical dodecahedral shape of pure ZIF-8 nanoparticles (Figure S1, Supporting Information online). The particle size is around 500 nm. The high-angle annular dark field (HADDF) and energy dispersive X-ray spectroscopy (EDX) diagrams confirmed the uniform distribution of C, N, O, Zn, and Fe (Figure 2b). The X-ray diffraction (XRD) result signifies the crystal structure of ZIF-8 [39], while the asterisk-labeled peaks clarify that the magnetic source may be Fe_3O_4 or $ZnFe_2O_4$ [40] (Figure 2c). The magnetization response measurements show that the saturation magnetization of Fe@ZIF-8 is 10.1 emu/g, uncovering the superparamagnetic feature of the nanoparticles (Figure 2d). As can be seen from the inset of Figure 2d, Fe@ZIF-8 particles could be well dispersed in the solution and can respond to a magnet, indicating the controllable magnetic actuation through a magnetic field. In order to verify whether the high surface area was maintained, the N_2 adsorption-desorption isotherm of Fe@ZIF-8 nanoparticles (Figure 2e) was measured at room temperature. It is worth noting that the Brunauer-Emmett-Teller (BET) specific surface area of them is 808.26 m^2/g, allowing for a high drug-carrying capacity.

2.2 Manipulation and multimode transformation of MMRSs

By virtue of the magnetic property, the MMRSs can be well manipulated in configurable microswarms under a magnetic field. The programmable magnetic field was generated by a three-dimensional Helmholtz coil setup (Figure S2), which could produce diverse magnetic field profiles to achieve the swarming behavior of MMRSs.

When a conical rotating field in the *x*-*z* plane was applied (see Supplementary Discussion Eq. S1, Supporting Information online), MMRSs formed chain-like swarms with direction along the short chain axis (Figure 3a and Movie S1, Supporting Information online). Specifically, the dispersed nanoparticles were assembled by the hydrodynamic flow under the conical magnetic field (H_c). Afterwards, the nanoparticles aligned along the short polarization axis and finally assembled into chain-like swarms once entering the magnetic dipole attraction range [19]. When a rotating magnetic field in the *x*-*y* plane was applied (see Supplementary Eq. S2), MMRSs exhibited vortex-like swarms from the initial status of dispersion (Figure 3b). For the rotating magnetic field (H_v), the originally monodisperse paramagnetic nanoparticles will form into rotating chains and generate eddies. Moreover, once the distance between the two rotating chains was less than a critical value (the ratio of the core radius of the vortices formed by the chains to the distance between the two vortices), the vortices promoted the rotating chains to merge into the vortex-like swarms [41].

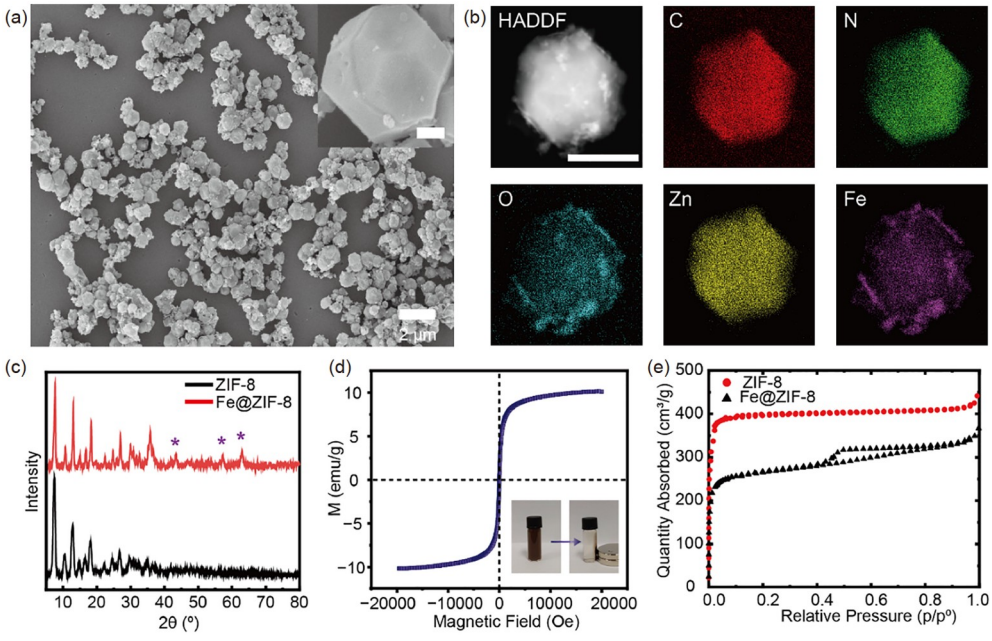

Figure 2 (a) SEM images of Fe@ZIF-8 nanoparticles. The scale bar of the inset image is 200 nm. (b) HAADF and EDX maps of a single Fe@ZIF-8 nanoparticle. The EDX maps show the C, N, O, Zn and Fe distribution in the crystal. The scale bar is 500 nm. (c) XRD pattern of ZIF-8 and Fe@ZIF-8 nanoparticles, respectively. The asterisks imply the peaks of Fe_3O_4 or $ZnFe_2O_4$. (d) Magnetization curves of Fe@ZIF-8 nanoparticles. The inset shows the excellent magnetic responsiveness of the nanoparticles. (e) N_2 absorption/desorption isotherm of ZIF-8 and Fe@ZIF-8 nanoparticles, respectively (color online).

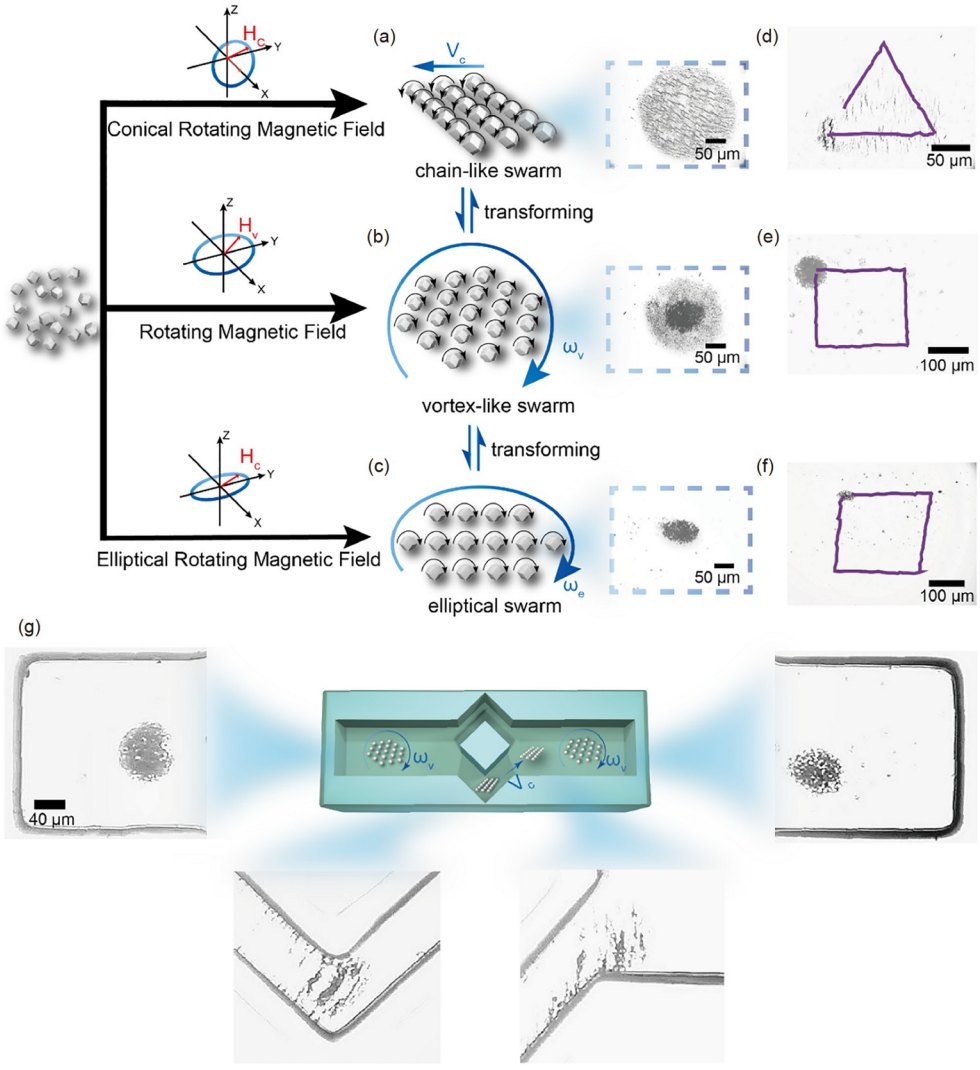

Figure 3 (a–c) Schematic of three microswarms configurations: chain-like swarms, vortex-like swarms and elliptical swarms under the discrete magnetic fields. (d) Triangle trajectory of the chain-like swarm (magnetic strength: 4 mT, frequency: 10 Hz). (e) Quadrangle trajectory of the vortex-like swarms (magnetic strength: 4 mT, frequency: 20 Hz). (f) Parallelogram trajectory of the elliptical swarms (magnetic strength: 10 mT, frequency: 10 Hz, field aspect ratio γ: 0.375). (g) The transformation between the vortex-like swarms and chain-like swarms when encountering a barrier (color online).

With respect to elliptical swarms (Figure 3c), the MMRSs along the long axis of the field were subject to larger inward forces, whereas the inward force was much weaker along the short axis. As a consequence, the swarm contracted along the long axis of the field and formed an elliptical pattern [24].

In addition, the collective motion of the above three MMRS swarms was further evaluated. Initially, solitary nanoparticles were observed. When the homologous magnetic fields were employed, the MMRSs transformed into the corresponding pattern intelligently (Movie S1). Notably, the length of the elliptical swarms was regulated by altering the field aspect ratio γ, which is the ratio of the short axis to the long axis of the elliptical field [24]. The moving directions of the three diverse MMRSs swarms were dexterously regulated depending on the adjustment of the yaw angle of the corresponding magnetic fields (Figure S3). Thus, they could be propelled exactly along the predetermined trajectory of a triangle, rectangle, and diamond and return to the original points, respectively (Figure 3d–f, Movie S2). Considering the complexity of blood vessels in the human body, once the vortex-like swarms could not disassemble without delay, the risk of undesired thrombosis dramatically increased. Therefore, the transformation between different MMRSs is desirable in practical biomedical applications. In this regard, a microchannel to mimic the limitations of physiological routes was designed to assess the swarm mode transformation capability (see Experimental Section). As shown in Figure 3g, when encountering an incommodious channel during the locomotion, the vortex-like MMRSs with a diameter of 20 μm can be programmed to convert its shape into chain-like mode before undergoing the resisting torque from the wall (Figure 3g and Movie S3), and subsequently re-

formed into vortex-like swarms. The reversible multimode transformations of the MMRSs indicate their superior environment adaptability and extraordinary flexibility.

2.3 Formation and navigated locomotion of vortex-like MMRSs

Considering the reliable maneuverability and universal applicability of the vortex-like configuration, we primarily applied the vortex-like MMRSs for later drug delivery investigations. The assembling properties of MMRSs under a magnetic field with various magnetic strengths and frequencies are shown in Figure 4a. As can be seen, the vortex-like MMRSs failed to assemble at all counts when the frequency of the magnetic field was below 2 Hz. With increasing frequency, the scattered nanoparticles assembled together to form vortex-like MMRSs with loss, which is marked as a red domain in Figure 4a. Only in the blue domain with higher frequency did the nanoparticles successfully assemble into vortex-like MMRSs, signifying the MMRSs reached the dynamic equilibrium [23]. Remarkably, the size of MMRSs could be easily tuned by varying the injection dose. As demonstrated in Figure 4b and Movie S4, the MMRSs with disparate sizes from 10 to 500 μm can be aggregated by a small magnet and accurately manipulated to move along the same trajectory. Moreover, this approach was relatively simple and convenient compared with adjusting the size of swarms through magnetic poles, although the accuracy was somewhat reduced [42], which plays a crucial role in regulating the drug loading dose on demand. Based on these experimental results, we expanded the precision manipulation demonstrations. The vortex-like MMRSs were navigated along the predesigned trajectories to depict the letters J, N, and U *via* tuning the yaw angle of the rotating magnetic field (Figure 4c and Movie S5), illustrating its remarkable controllability. To adapt to the intricate biological environment, the locomotion of the MMRSs continued to be assessed with a microchannel (Figure 4d and Movie S6), which was utilized to simulate the blood vessels during the process of drug delivery in the human body. The vortex-like MMRSs were fleetingly and accurately steered to the allocated spot under the magnetic motivation despite multiple side roads. Since the external nanoparticles in the swarms are less attracted to the vortex and the base viscosity is high, there will be some loss in the overall quantity. By calculating the change in the swarm's area, the loss was estimated to be approximately 20.67%. The aforementioned phenomena further elucidate that vortex-like MMRSs possess prominent actuation, modifiability, and blameless stability, making targeted drug delivery possible.

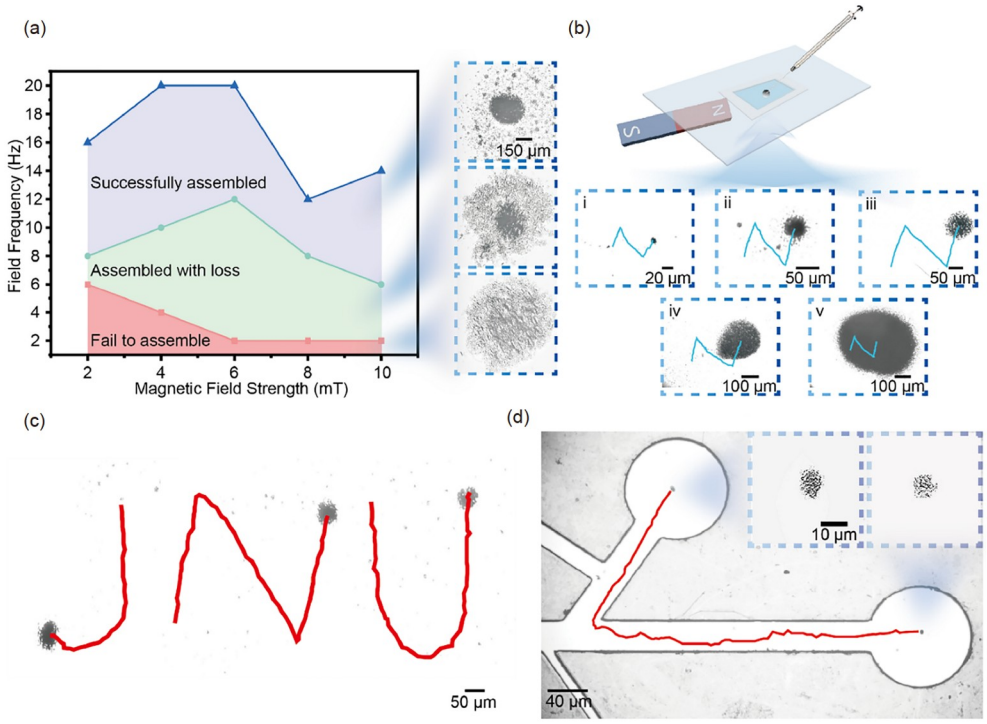

Figure 4 (a) The phase diagram of successfully assembling, assembling with loss and failing to assemble the vortex-like swarms from 2 to 10 mT. The blue region indicates the range that the vortex-like swarms successfully assembled, the red region represents the procedure of assembling with loss, and the gray region indicates the range that the vortex-like swarms failed to assemble. (b) The trajectory of the different-sized vortex-like swarms. The strength and frequency of the rotating magnetic field for the construction of different-sized swarms are diverse. (c) The navigated locomotion trajectory of the vortex-like swarms, spelling the alphabets of "JNU". The strength of the rotating magnetic field is 4 mT and the frequency is 20 mT. (d) The manipulated locomotion trajectory in the microchannel of the vortex-like swarms. The strength of the rotating magnetic field is 6 mT and the frequency is 20 Hz (color online).

2.4 Cytotoxicity and pH-responsive drug release *in vitro*

In order to achieve targeted drug delivery, in addition to excellent controllability, biocompatibility, drug-loading and responsive releasing are also significant properties of MMRSs. Therefore, we evaluated the drug loading capacity of the nanoparticles by taking the conventional DOX as the model anticancer drug. As shown in Figure 5a, the UV-vis absorption spectroscopy measurement was applied to quantify the concentration of DOX solutions (see standard curve in Figure S4). The drug loading efficiency was calculated (see Experimental Section Eq. S3 and Eq. S4) to be 68.43%. This high loading efficacy can be attributed to the coordination bonding of Zn(II)-DOX [43] and the high specific surface area of Fe@ZIF-8 nanoparticles.

For the biological applications, biocompatibility is an essential consideration. A CCK-8 assay was applied to assess the biocompatibility of the Fe@ZIF-8 nanoparticles (see Experiments Section). As shown in Figure 5b, the nanoparticles show inapparent cytotoxicity to normal cells after being cultured with Fibroblasts for 24 h (Figure S5) when the concentration was no more than 30 μg/mL. Hence, the Fe@ZIF-8 nanoparticles are biocompatible and appropriate as drug carriers. Moreover, the property of pH-responsive decomposition, which is crucial for drug release, was explored. Figure 5c shows the drug releasing dynamics at different pH conditions, which rapidly ramped up within the first 10 h and gradually saturated. Meanwhile, the drug release speed was much higher in acidic conditions (pH 5.5) than in physiological conditions (pH 7.4) due to the pH-sensitive decomposition. This result indicates the drug in MMRSs might be released on-demand near the targeted cancer location through pH-triggered degradation to minimize the required dosage, while maintaining greater stability under physiological conditions.

Subsequently, the DOX-loaded MMRSs were incubated with human breast cancer cells (MCF-7), taking Fe@ZIF-8 and blank as controls. After 48 h of treatment, the viability of the cancer cells incubated with DOX@Fe@ZIF-8 radically reduced compared with the other two controlling groups (Figure 5d). The experiment was conducted under a fluorescence microscope with LIVE/DEAD staining of cancer cells, as shown in Figure 5e. All the results confirmed that MMRSs can be a promising candidate to kill tumor cells due

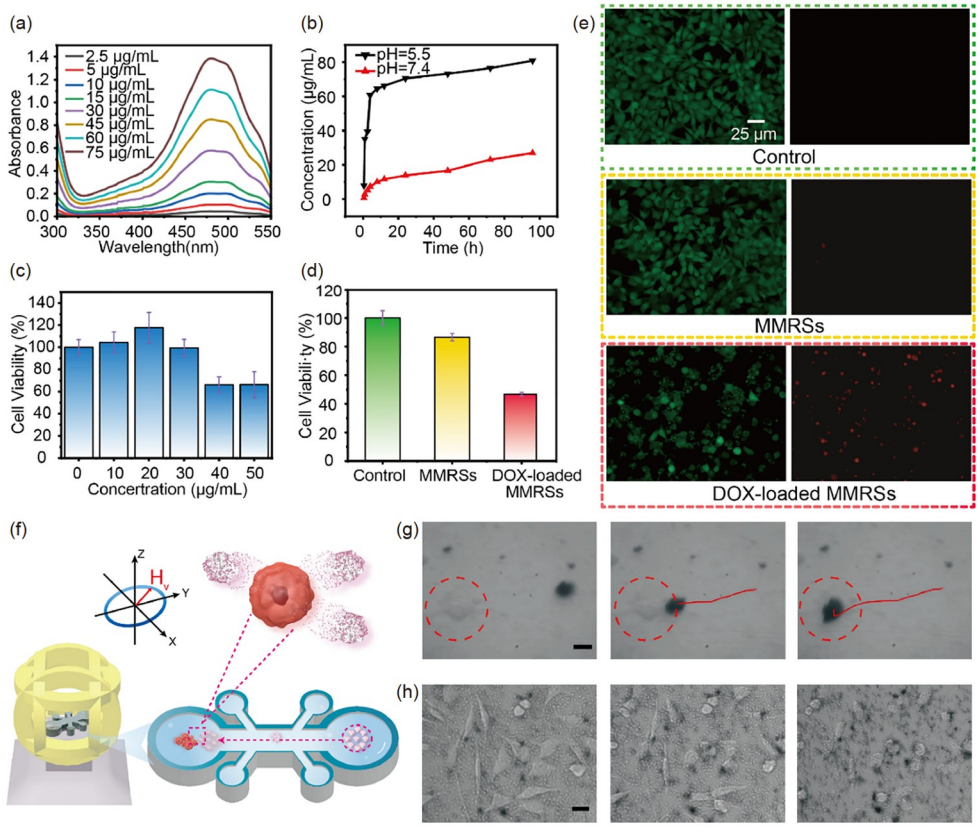

Figure 5 (a) UV-vis absorption spectroscopy with different DOX concentrations. (b) The viability of normal cells (Fibroblasts) incubated with the Fe@ZIF-8 of different concentrations. (c) DOX release properties of DOX@Fe@ZIF-8 nanoparticles in PBS at pH 7.4 and 5.5. (d) The viability of human breast cancer cells (MCF-7) with Fe@ZIF-8, DOX@Fe@ZIF-8 and control after incubation for 48 h. (e) Live/Dead staining images of MCF-7 cancer cells incubated with Fe@ZIF-8 and DOX@Fe@ZIF-8, taking blank as control. (f) Schematic illustration of the DOX-loaded MMRSs to kill MCF-7 cancer cells under magnetic propulsion. (g) Time-lapse images of the DOX-loaded MMRSs manipulated toward the targeted MCF-7 cells in the DMEM cell culture medium under a transversal rotating magnetic field. The strength of the applied magnetic field is 10 mT, and the frequency is 5 Hz. The scale bar is 5 μm. (h) Time-lapse images of the MCF-7 cancer cells incubated with DOX-loaded MMRSs. The scale bar is 25 μm (color online).

to their low cytotoxicity, high drug capacity, and pH-sensitive release ability.

2.5 Stability and antitumor effect of DOX@MMRSs *in vivo*

To investigate the potential premature release of DOX@MMRSs *in vivo*, we employed a subcutaneous tumor model. Fluorescein isothiocyanate (FITC) was used as a drug model to load into the MMRSs for *in vivo* imaging. As shown in Figure 6a, the fluorescence intensity of FITC@MMRSs at the tumor site exhibited a significant reduction, while the fluorescence intensity of MMRSs at the tumor-free site remained relatively constant, confirming the stability of MMRSs in normal physiological conditions and further validating their pH-responsive drug release capability. Moreover, the antitumor effect of DOX@MMRSs *in vivo* was comprehensively evaluated. As depicted in Figure 6b, the mice with tumors were subjected to treatment with magnetically controlled DOX@MMRSs or other control groups and subsequently analyzed. The results presented in Figure 6c and d reveal that magnetically controlled DOX@MMRSs exhibited the most effective inhibition of T24 tumors, as evidenced by the smallest tumor volume and the lightest tumor weights among the four groups. Additionally, the body weight of the mice (Figure 6e) showed negligible fluctuations, underscoring the remarkable biocompatibility of MMRSs *in vivo*.

3 Conclusions

In summary, we proposed targeted cancer therapy by using the magnetic microrobot swarms based on metal-organic frameworks (MOFs). A one-pot mineralization method was deployed to fabricate the hybrid DOX@Fe@ZIF-8 nanoparticles, generating high drug loading capacity and magnetic properties. The microrobot swarms exhibit intelligent multi-mode transformations, including vortex-like, chain-like, and elliptical configurations, in response to programmable magnetic fields, which provides a solid foundation for medical applications. Moreover, we demonstrate the low toxicity and pH-responsive release capacity of DOX-loaded microrobot swarms in a simulated living organism-environment, where the generated MMRSs size can be modulated from ten to several hundreds of micrometers as required, making them suitable for targeted chemotherapy. The anticancer efficacy of the magnetically manipulated

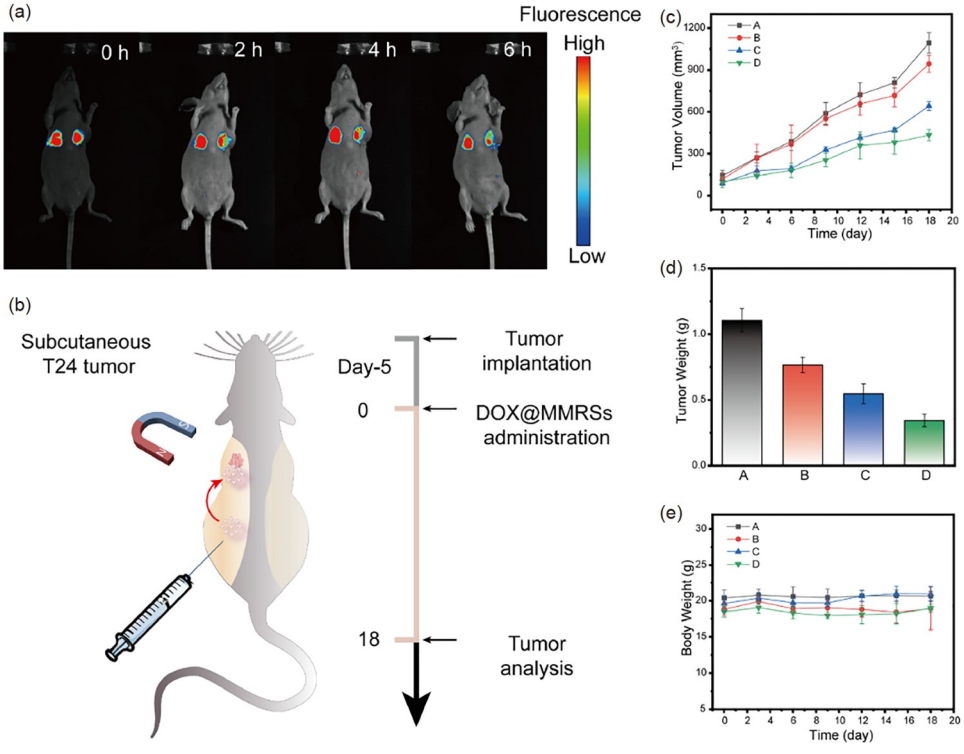

Figure 6 (a) Fluorescence images depicting FITC-labeled MMRSs on both sides of the mouse after different incubation durations. The injection area on the left side of the mouse is tumor-free, while the right side corresponds to the tumor site. (b) Schematic of establishing, treating and analyzing subcutaneous T24 tumor model. (c) The tumor volume variations of tumor-bearing mice that were intratumorally injected with PBS (A), MMRSs (B), DOX@MMRSs (C), and magnetically controlled DOX@MMRSs (D) near the tumor site during the treatment process (n = 3; means ± SD). As for the magnetically controlled DOX@MMRSs group, the magnet was applied to control the DOX@MMRSs to achieve the tumor site. (d) The weights of excised tumors from mice at the end of treatment with magnetically controlled DOX@MMRSs and other groups (n = 3; means ± SD). (e) The body weight of tumor-bearing mice under different intravenous administrations during the treatment process (n = 3; means ± SD) (color online).

DOX@MMRSs was further demonstrated in mice with subcutaneous T24 tumors. This work also suggests the potential of combining microrobot swarms with responsive MOF-based materials for targeted drug delivery. The swarms can enhance medical imaging contrast, enabling real-time control and monitoring *in vivo* using techniques such as magnetic resonance imaging (MRI), and ultrasound imaging [44–46], thus making magnetic microrobot swarms a promising candidate for clinical applications.

Acknowledgements This work was supported by the National Natural Science Foundation of China (22275073, 22005119, 21731002, 21975104 22150004), the Guangdong Major Project of Basic and Applied Research (2019B030302009), the Guangdong Basic and Applied Basic Research Foundation (2020A1515110404), the Guangzhou Basic and Applied Basic Research Foundation (2024A04J3597, 202102020444), and the Fundamental Research Funds for the Central Universities (21622409).

Conflict of interest The authors declare no conflict of interest.

Supporting information The supporting information is available online at chem.scichina.com and link.springer.com/journal/11426. The supporting materials are published as submitted, without typesetting or editing. The responsibility for scientific accuracy and content remains entirely with the authors.

1 Wang H, Pumera M. *Chem Rev*, 2015, 115: 8704–8735
2 You M, Chen C, Xu L, Mou F, Guan J. *Acc Chem Res*, 2018, 51: 3006–3014
3 Wang J, Xiong Z, Liu M, Li X, Zheng J, Zhan X, Ding W, Chen J, Li X, Li XD, Feng SP, Tang J. *ACS Nano*, 2020, 14: 3272–3280
4 Ussia M, Urso M, Kratochvilova M, Navratil J, Balvan J, Mayorga-Martinez CC, Vyskocil J, Masarik M, Pumera M. *Small*, 2023, 19: 2208259
5 Liu Z, Li T, Li N, Wang Y, Chen L, Tang X, Wan M, Mao C. *Sci China Chem*, 2022, 65: 989–1002
6 Liu K, Liu Q, Yang J, Xie C, Wang S, Tong F, Gao J, Liu L, Ye Y, Chen B, Cai X, Liu Z, Li Z, Peng F, Tu Y. *ACS Nano*, 2023, 17: 300–311
7 Law J, Wang X, Luo M, Xin L, Du X, Dou W, Wang T, Shan G, Wang Y, Song P, Huang X, Yu J, Sun Y. *Sci Adv*, 2022, 8: eabm5752
8 Kong L, Mayorga-Martinez CC, Guan J, Pumera M. *Small*, 2020, 16: 1903179
9 Li W, Wu C, Xiong Z, Liang C, Li Z, Liu B, Cao Q, Wang J, Tang J, Li D. *Sci Adv*, 2022, 8: eade1731
10 Urso M, Ussia M, Pumera M. *Nat Rev Bioeng*, 2023, 1: 236–251
11 Zhou H, Mayorga-Martinez CC, Pané S, Zhang L, Pumera M. *Chem Rev*, 2021, 121: 4999–5041
12 Xu T, Hao Z, Huang C, Yu J, Zhang L, Wu X. *IEEE ASME Trans Mechatron*, 2022, 27: 4327–4338
13 Akolpoglu MB, Alapan Y, Dogan NO, Baltaci SF, Yasa O, Aybar Tural G, Sitti M. *Sci Adv*, 2022, 8: eabo6163
14 Xu L, Mou F, Gong H, Luo M, Guan J. *Chem Soc Rev*, 2017, 46: 6905–6926
15 Gao Y, Xiong Z, Wang J, Tang J, Li D. *Nano Res*, 2022, 15: 5355–5375
16 Kochergin YS, Villa K, Novotný F, Plutnar J, Bojdys MJ, Pumera M. *Adv Funct Mater*, 2020, 30: 2002701
17 Ye J, Fu Q, Liu L, Chen L, Zhang X, Li Q, Li Z, Su L, Zhu R, Song J, Yang H. *Sci China Chem*, 2021, 64: 2218–2229
18 Wang W, Castro LA, Hoyos M, Mallouk TE. *ACS Nano*, 2012, 6: 6122–6132
19 Xie H, Sun M, Fan X, Lin Z, Chen W, Wang L, Dong L, He Q. *Sci Robot*, 2019, 4: eaav8006
20 Law J, Chen H, Wang Y, Yu J, Sun Y. *Sci Adv*, 2022, 8: eade3161
21 Yu J, Wang B, Du X, Wang Q, Zhang L. *Nat Commun*, 2018, 9: 3260
22 Wang J, Xiong Z, Tang J. *Adv Intelligent Syst*, 2021, 3: 2000170
23 Yu J, Jin D, Zhang L. Mobile paramagnetic nanoparticle-based vortex for targeted cargo delivery in fluid. In: IEEE International Conference on Robotics and Automation (ICRA). New York: IEEE, 2017. 6594–6599
24 Chen H, Wang Y, Liu Y, Zou Q, Yu J. *ACS Nano*, 2022, 16: 16281–16291
25 Yang S, Wang Q, Jin D, Du X, Zhang L. *ACS Nano*, 2022, 16: 19025–19037
26 Wu M, Yang Y. *Adv Mater*, 2017, 29: 1606134
27 Yang J, Yang Y. *Small*, 2020, 16: 1906846
28 Yang J, Dai D, Zhang X, Teng L, Ma L, Yang YW. *Theranostics*, 2023, 13: 295–323
29 Wang CY, Qin JC, Yang YW. *J Agric Food Chem*, 2023, 71: 01094
30 Furukawa H, Cordova KE, O'Keeffe M, Yaghi OM. *Science*, 2013, 341: 1230444
31 Gao L, Chen Q, Gong T, Liu J, Li C. *Nanoscale*, 2019, 11: 21030–21045
32 Zheng H, Zhang Y, Liu L, Wan W, Guo P, Nyström AM, Zou X. *J Am Chem Soc*, 2016, 138: 962–968
33 Wang H, Li T, Li J, Tong W, Gao C. *Colloids Surfs A-Physicochem Eng Aspects*, 2019, 568: 224–230
34 Jin Y, Guo Y, Yang J, Chu X, Huang X, Wang Q, Zeng Y, Su L, Lu S, Wang C, Yang J, Qu J, Yang Y, Wang B. *Adv Mater*, 2023, 35: 2209690
35 Chen H, Yang J, Sun L, Zhang H, Guo Y, Qu J, Jiang W, Chen W, Ji J, Yang Y, Wang B. *Small*, 2019, 15: 1903880
36 Wang X, Chen X, Alcântara CCJ, Sevim S, Hoop M, Terzopoulou A, de Marco C, Hu C, de Mello AJ, Falcaro P, Furukawa S, Nelson BJ, Puigmartí-Luis J, Pané S. *Adv Mater*, 2019, 31: 1901592
37 Terzopoulou A, Wang X, Chen X, Palacios-Corella M, Pujante C, Herrero-Martín J, Qin X, Sort J, deMello AJ, Nelson BJ, Puigmartí-Luis J, Pané S. *Adv Health Mater*, 2020, 9: 2001031
38 Terzopoulou A, Hoop M, Chen X, Hirt AM, Charilaou M, Shen Y, Mushtaq F, del Pino AP, Logofatu C, Simonelli L, de Mello AJ, Doonan CJ, Sort J, Nelson BJ, Pané S, Puigmartí-Luis J. *Angew Chem Int Ed*, 2019, 58: 13550–13555
39 Hoop M, Walde CF, Riccò R, Mushtaq F, Terzopoulou A, Chen XZ, deMello AJ, Doonan CJ, Falcaro P, Nelson BJ, Puigmartí-Luis J, Pané S. *Appl Mater Today*, 2018, 11: 13–21
40 Li J, Li T, Gorin D, Kotelevtsev Y, Mao Z, Tong W. *Colloids Surfs A-Physicochem Eng Aspects*, 2020, 601: 124990
41 Yu J, Yang L, Zhang L. *Int J Robot Res*, 2018, 37: 912–930
42 Wang X, Wang T, Chen X, Law J, Shan G, Tang W, Gong Z, Pan P, Liu X, Yu J, Ru C, Huang X, Sun Y. *ACS Nano*, 2022, 16: 10824–10839
43 Chen G, Yu B, Lu C, Zhang H, Shen Y, Cong H. *CrystEngComm*, 2018, 20: 7486–7491
44 Wang Q, Zhang L. *ACS Nano*, 2021, 15: 149–174
45 Martel S, Felfoul O, Mathieu JB, Chanu A, Tamaz S, Mohammadi M, Mankiewicz M, Tabatabaei N. *Int J Robotics Res*, 2009, 28: 1169–1182
46 Wang Q, Yang L, Yu J, Vong C I, Chiu P W Y, Zhang L. Magnetic navigation of a rotating colloidal swarm using ultrasound images. In: IEEE International Conference on Intelligent Robots and Systems (IROS). New York: IEEE, 2018. 5380–5385